The International Journal of Advanced Manufacturing Technology (2023) 125:1271–1287
https://doi.org/10.1007/s00170-022-10704-3

ORIGINAL ARTICLE

Effects of double pulse welding on microstructure, texture, and fatigue behavior of DP590 steel resistance spot weld

Imtiaz Ali Soomro[1,2] · **Srinivasa Rao Pedapati**[1] · **Mokhtar Awang**[1] · **Mohammad Azad Alam**[1]

Received: 26 July 2022 / Accepted: 11 December 2022 / Published online: 6 January 2023

Abstract

In the present study, dual-phase (DP590) steel sheets were joined using single-pulse and double-pulse resistance spot welding in lap joint configuration. Effects of the welding method on microstructure, texture, tensile shear properties (load carrying and energy absorption capacity), and fatigue strength of welded joints were investigated. Tensile shear test results showed that double-pulse weld exhibits an average of 15.6% and 83.1% higher peak load and failure energy, respectively than single-pulse weld. Fatigue test results showed that double-pulse welds withstand 10.8%, 22.7%, 1.8%, 158.7%, and 20.2% higher number of cycles than single-pulse welds at an applied load of 2.3, 2.76, 3.45, 4.6, and 8.1 kN, respectively. The better mechanical performance of the double pulse spot welds is attributed to the large nugget size resulting in higher bonding area, the tough microstructure of the nugget consisting of tempered martensite structure, acicular ferrite, and Widmanstätten ferrite, and the formation of randomly orientated grains with a high fraction of high angle boundaries in the fusion zone, which resulted in improved resistance to crack propagation during mechanical loading.

Keywords Resistance spot welding · Dual-phase steel · Microstructure · Texture · Tensile shear load · Fatigue test

Abbreviations

SPW	Single pulse welding
DPW	Double pulse welding
DP	Dual phase
FZ	Fusion zone
HAZ	Heat affected zone
CGHAZ	Coarse grain heat affected zone
FGHAZ	Fine grain heat affected zone
SCHAZ	Subcritical heat affected zone
RSW	Resistance spot welding
PAG	Prior austenite grain
LAGBs	Low angle grain boundaries
HAGBs	High angle grain boundaries
PF	Pullout failure
IF	Interfacial failure
FL	Failure location

1 Introduction

Over the past two decades, lowering carbon emissions, increasing passenger safety standards, and high fuel efficiency have been the main drivers in designing automobiles. A key strategy to reduce fuel consumption has been identified as vehicle weight reduction using light-weight structural materials. At the same time, vehicle structures that have a higher energy absorption capacity in crash situations are required for passenger safety. Advanced high-strength steels (AHSS) have been developed to meet the stringent requirements of the automotive industry [1]. AHSS are multiphase alloys that contain martensite, bainite, and/or retained austenite in sufficient quantities to generate unique mechanical properties. Dual-phase (DP) steels are members of the first-generation AHSS. DP steels possess high strength and excellent ductility. Apart from that, high strain hardening rate, low yield to tensile strength ratio, continuous yielding behavior, and good resistance to fatigue failure are other significant features of DP steels. The combination of these superior mechanical

✉ Imtiaz Ali Soomro
imtiaz_17007503@utp.edu.my;
imtiaz.soomro@faculty.muet.edu.pk

[1] Department of Mechanical Engineering, Universiti Teknologi PETRONAS, 32610 Seri Iskandar, Perak Darul Ridzuan, Malaysia

[2] Department of Metallurgy and Materials Engineering, Mehran University of Engineering and Technology, Jamshoro 76062, Sindh, Pakistan

properties is the synergistic effect of the unique microstructure of DP steels, composed of a soft ferrite matrix embedded with hard martensite islands [2]. Ferrite in DP steel provides excellent ductility, whereas martensite islands contribute to strength. Typically, martensite volume varies between 15–80%. A linear relationship exists between the volume fraction of martensite and the strength of DP steel grades [3]. The composite microstructure enables DP steels to achieve an ultimate tensile strength in the range of 500–1200 MPa, which allows for a broad range of applications in car body structures such as bumpers, B-pillars, side-impact beams, etc. [4].

Recent trends towards integrating DP steels into the automotive body structure have accentuated demands on their resistance to spot weldability. In automotive industry, resistance spot welding (RSW) is the most widely used method to join sheet metal parts [5]. The mechanical properties of the automotive assemblies depend not only on sheet material but also on the mechanical behaviors of the spot-welded joints connecting them [6]. Among various design factors of spot welds for vehicle structures, the most important is the ability to sustain the various types of dynamic loads. Particularly, performance under impact and fatigue is crucial [7]. Most fatigue failures in a vehicle body structure occur at or around the spot welds. The majority of spot weld failures in automobiles occur due to cyclic loading in the form of vibrations [8]. Although spot weld fatigue failure is a local phenomenon, the failure can also affect the vehicle's stiffness and crash performance on a global level [8, 9]. Miller et al. [10] showed that fatigue crack also reduced the static and impact performance of the spot weld. Kim et al. [11] found that the fatigue strength of a high-strength steel resistance spot weld was only 2.5% of the maximum static cross-tension strength. Therefore, preventing spot welds fatigue failure is the foremost design requirement.

About 2000–5000 spot welds are made in a typical modern car body to connect structural assemblies. During resistance spot welding of DP steels, a brittle martensitic structure is formed in weldment which degrades the mechanical properties via promoting interfacial failure [12, 13] Chabok et al. [14] showed that DP1000 steel resistance spot weld exhibited low fracture strength due to the martensitic structure of the fusion zone, thus reducing the load-carrying capacity of the weld.

Tempering the martensite via applying a secondary pulse current after the first melting pulse current is considered a new pathway to increase the fracture toughness of automotive steel resistance spot weld and to alleviate the problem of high sensitivity to brittle interfacial fracture [15, 16]. Many researchers [17–20] have shown that the static tensile strength of resistance spot welds of automotive steels can be improved via using a double-pulse RSW process. However, the fatigue strength of resistance spot weld is equally important as static tensile strength. The microstructural changes imparted during double pulse resistance spot welding can affect the fatigue life of the weld. However, no studies have been conducted so far to determine the effect of double pulsing on the fatigue strength of automotive steel resistance spot welds. Therefore, the present study investigates the fatigue behavior of DP590 steel resistance spot welds fabricated via the double RSW method.

2 Experimental

2.1 Material

In the present work, a cold-rolled zinc-coated DP590 steel sheet with a thickness of 1.8 mm is used as base metal (BM). The mechanical properties and chemical composition of the base metal are given in Table 1. The base metal microstructure is shown in Fig. 1.

2.2 Welding procedures

Resistance spot welding was performed using a semi-automatic, alternating current type machine (model: *WIM* JPC 100). Welding was conducted using Cu-Cr alloy truncated cone-shaped electrodes with 8 mm face diameter and 45° bevel angle. Two RSW methods are used in the present investigation: conventional single-pulse welding (SPW) and double-pulse welding (DPW). Figure 2 shows the schematic illustration of SPW and DPW methods. SPW method consists of only one pulse current. This method aims to produce a spot weld with a minimum nugget size following the $5t^{0.5}$ (where t is sheet thickness and D is nugget size). DPW method consists of two pulse currents. After completing the first pulse current, the weld joint was reheated by applying a

Table 1 Mechanical properties and elemental composition of base metal

Mechanical properties					
Yield strength 440 MPa	Tensile strength 694 MPa			Elongation 11.58%	
Chemical composition					
0.09% C	0.388% Si	1.7% Mn	0.003% Cr	0.0301% Al	Balance Fe

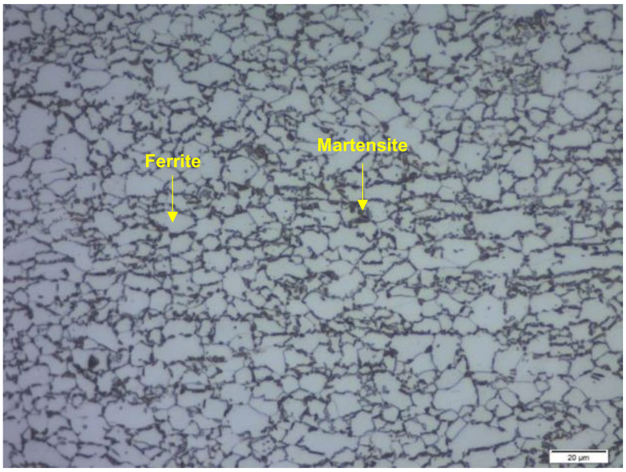

Fig. 1 Microstructure of base metal showing ferrite (light) and martensite (dark) phases

second pulse current after allowing a specific cooling time. This method aims to reduce the brittleness of the weld joint.

2.3 Microhardness and microstructure characterization

Microhardness testing was performed using a Vickers microindentation machine (model: Lecon LM-247AT, USA) to evaluate the weld brittleness. Microhardness tests were performed at an applied load of 200 g and loading time of 15 s across the weld on well-prepared metallographic specimens. Weld microstructure was examined using an optical microscope (BX51M, Olympus Japan) and a scanning electron microscope (VEGA3, TESCAN Czech Republic). Samples for microstructure observation were prepared using a standard metallographic procedure and then etched in 2% Nital reagent. Weld macrostructures were also revealed under a stereomicroscope (Leica EZ4HD, Germany).

2.4 Mechanical testing

Quasi-static lap tensile shear tests were performed at room temperature on a servohydraulic universal testing machine (ZwickRoell HA50, Germany) with a 50 kN loading capacity at a crosshead speed of 10 mm/min. Specimens for the tensile shear tests were prepared according to JIS Z-3136 (1999) standard. Supporting shims of the same thickness as that of the base metal sheet were added at the grip section of the specimen to reduce the sheet bending and nugget rotation. Load-controlled axial fatigue tests were conducted at room temperature on a servohydraulic testing machine (model: Servopulser EHF-LV020K1-020, Shimadzu Corporation, Japan) with 20 kN maximum loading capacity. Specimens were prepared according to ISO 14324:2003 standard. Shims were spot-welded at both ends of the specimen to minimize the flexural moment during the cyclic loading. A constant amplitude cyclic loading with a sinusoidal wave (tensile-tensile loading) at a frequency of 15 Hz and load ratio of $R=0.1$ was used. The applied fatigue loads were kept well below the average tensile shear peak load of the weld joint. The fatigue test was terminated when the first crack initiated from one side of the nugget and propagated through thickness and became visible from the other side of the nugget or when the required number of cycles was achieved by the specimen. The fractography of the tensile shear and fatigue-tested specimens was performed using a field emission scanning electron microscope (FESEM, Carl Zeiss Supra55 VP) and stereomicroscope.

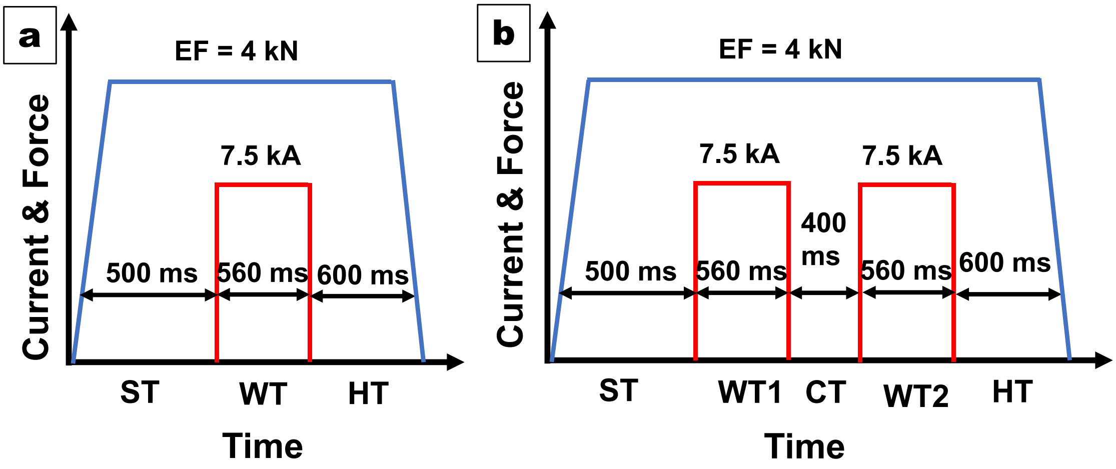

Fig. 2 RSW schemes used in the present investigation **a** single pulse welding and **b** double pulse welding. Note: ST is squeeze time, WT is welding time, CT is cooling time, HT is holding time, and EF is electrode force

2.5 Texture characterization

The texture of the various zones of the weld joint was examined using orientation imaging microscopy (OIM). The OIM characterization was carried out using a Schottky variable pressure field emission scanning electron microscope (VP-FESEM) (model: Hitachi SU5000) equipped with an electron backscatter diffraction (EBSD) detector (model: EDAX Hikari). EBSD scan was performed at acceleration voltage of 20 kV, a working distance of 17.5 mm, a tilt angle of 70°, and a step size of 0.10 µm. Analysis of orientation data was performed using TSL OIM Analysis™ (V8.6) software. EBSD scans were carried out on the TD-RD axis (where TD is the transverse direction and RD is the rolling direction of the specimen).

2.6 Nanoindentation

Nanoindentation was performed on a well-prepared metallographic sample using a TriboIndenter (Bruker Hysitron TI950) equipped with a scanning probe microscope (SPM). The Berkovich indenter with Young's modulus of 1140 GPa, Poisson's ratio of 0.07, half-angle of 65.27°, and the inclined angle of 142.3° was employed for indentation. The indenter was calibrated using a standard fused quartz specimen. The indentation was performed at a loading rate of 2 mN/s, and a loading–unloading period of 20 s was set up with a loading time of 9 s, a holding time of 2 s, and an unloading time of 9 s. After performing several trials at different load conditions, a constant load of 3000 µN was established. Nanoindentation was conducted to assess the elastic modulus (E) and nanohardness (H) of different regions of the weld. Nanohardness and elastic modulus were determined according to Oliver and Pharr method [21]. An average of two readings from the same phase/location was considered.

3 Results and discussion

3.1 Macro/micro-scale metallurgical characteristics of the welds

Figure 3 shows the macrostructural view of spot-welded joints. As can be seen that joints show three distinct regions, i.e., fusion zone (FZ), heat affected zone (HAZ), and base metal (BM). The fusion zone melted and solidified during welding while the surrounding HAZ experienced only microstructure changes. BM remained unaffected during the welding process. The nugget diameter (D) refers to the width of the elliptical-shaped nugget present in the central portion of the joint. It can be observed that the nugget diameter of the weld made via the DPW method is 13.8% higher compared to the weld made via the SPW method. It is well known that the nugget diameter of resistance spot weld increases with increasing welding heat input. In RSW, the heat is generated due to ohmic heating, defined as $H = I^2Rt$ (where H is the amount of heat generated, I is the welding current, R is resistance, and t is the welding time). The relationship indicates that the heat generation increase as the welding current and time increase. Moreover, it also shows that welding current makes a higher contribution to heat generation. During the double pulse welding method, two identical welding currents of 7.5 kA were applied compared to one welding current of 7.5 kA in the single pulse welding method for the same time duration; thus double pulse weld joint experienced greater heat input. Therefore, the nugget diameter of the double pulse weld joint increased due to the higher melting of the base metal. A detailed analysis of the mechanism of weld nugget enlargement during double pulse RSW of DP590 steel is discussed in Ref [22].

Figure 4 shows the microstructure of different regions of the single-pulse weld joint. Figure 4a shows the microstructure of FZ, which consists of large columnar grains perpendicular to the weld centerline. This is because liquid metal solidified along the direction of maximum heat flow, i.e., towards electrodes. A higher magnification optical micrograph shown in Fig. 4b exhibits the lath martensite structure in the FZ, which is a characteristic structure of most automotive steel resistance spot weld joint. Rapid cooling of the weld due to water-cooled copper electrodes promoted the martensite formation in FZ [23]. Figure 4c shows the microstructure of CGHAZ, which exhibits coarse packets of lath martensite. In this region, the temperature exceeded Ac3 (upper critical temperature of the Iron-carbon phase diagram), due to which complete austenite formed promptly with grain growth. Upon rapid cooling, the coarse grains of austenite transformed into coarse grains of martensite. Figure 4d shows the microstructure of FGHAZ, which exhibits fine packets of lath martensite. In this region, although the temperature exceeded Ac3 resulting in complete austenite formation, the lower temperature than CGHAZ limits the grain growth. Upon rapid cooling, fine packets of lath martensite formed. Figure 4e shows the microstructure of SCHAZ consisting of fine grains of ferrite and tempered martensite. During welding, the temperature in this weld region remained below Ac1 (lower critical temperature of the iron-carbon phase diagram) due to a sufficiently large distance from the FZ boundary where the effect of heat becomes negligible; hence no phase transformation occurred. However, some tempering of the martensite present in base metal occurred. Tempering of martensite in HAZ of DP steels resistance spot weld is also reported in previous works [24, 25].

Figure 5 shows the microstructure of different regions of the double-pulse weld joint. Figure 5a shows the microstructure of FZ, which exhibits columnar grains similar

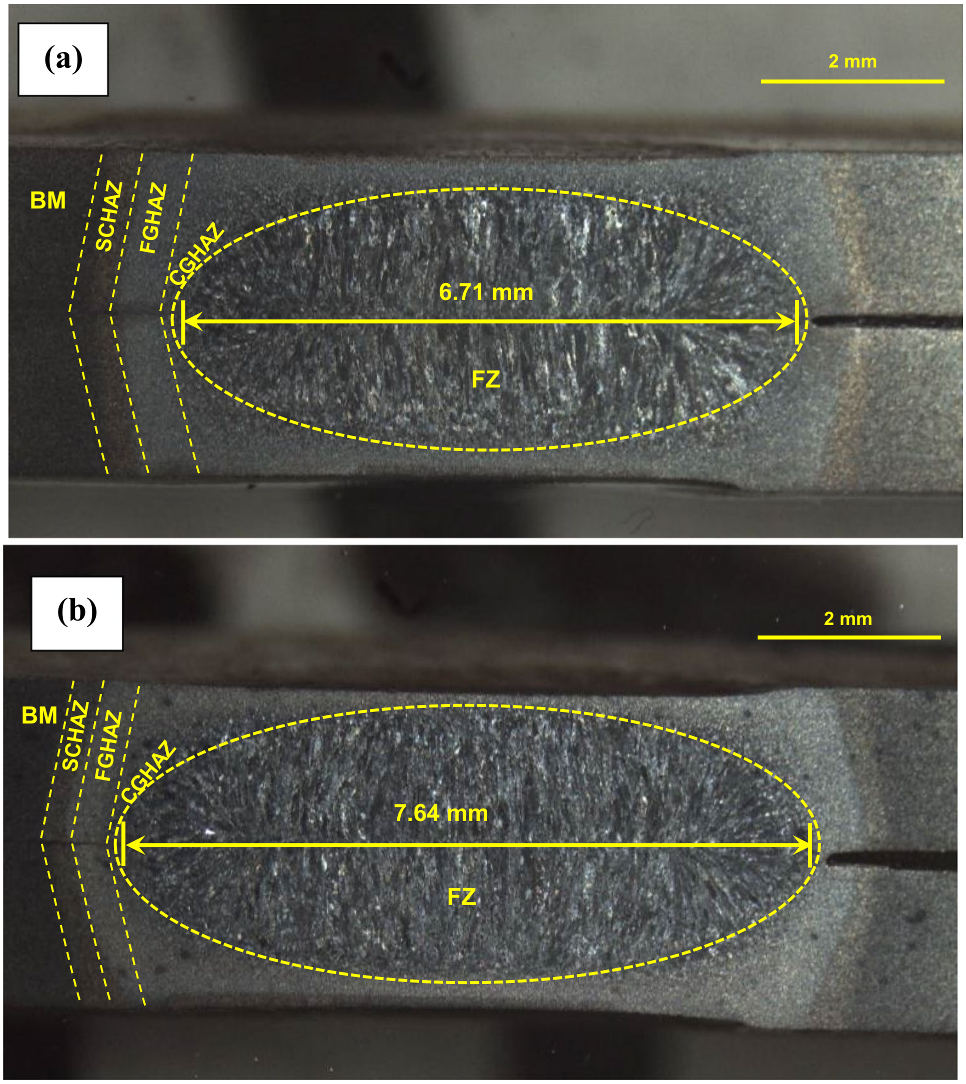

Fig. 3 Weld cross-sections of **a** single pulse welded joint and **b** double pulse welded joint

to the single-pulse weld joint. However, these columnar grains consist of different phases, i.e., tempered martensite consisting of carbides distributed in ferrite matrix, acicular ferrite (AF) visible as randomly oriented thin needles and Widmanstätten ferrite (WF) appears as lengthy thin plates, as can be observed in higher magnification micrograph shown in Fig. 5b. Tempered martensite formed due to rapid heating of weld during the secondary heating cycle resulting in carbide precipitation. Acicular ferrite and Widmanstätten ferrite are assumed to be formed due to the recrystallization of tempered martensite. During secondary heating, the temperature reached slightly above Ac3 in some local areas, resulting in austenite formation, which upon cooling, transformed into acicular ferrite and Widmanstätten ferrite [26, 27]. Recrystallization of tempered martensite can be attributed to non-homogeneous temperature distribution in the weldment during the secondary heating cycle. The martensite-austenite reverse transformation in some local areas of the fusion zone occurred by following mentioned sequence of events;

$$\rightarrow a_{C-depleted} + a_{C-rich} \rightarrow a_{C-depleted} + Fe_3C \rightarrow \gamma$$

where à is as-quenched martensite, $\alpha_{\text{C-depleted}}$ is low carbon ferrite, $\alpha_{\text{C-rich}}$ is high carbon ferrite, Fe_3C is cementite, and γ is austenite. During the initial stages of rapid heating, the carbon started to diffuse out of the martensite lattice resulting in low and high-carbon ferrite regions. With the progress of tempering, carbon-rich ferrite transformed into cementite which, along with low-carbon ferrite, transformed into austenite [28]. The microstructure of CGHAZ and FGHAZ (refer to Fig. 5c, d) shows only tempered martensite and the microstructure of SCHAZ shows ferrite and severely tempered (refer to Fig. 5e). The significant tempering of martensite in HAZ of double pulse weld joint can be attributed

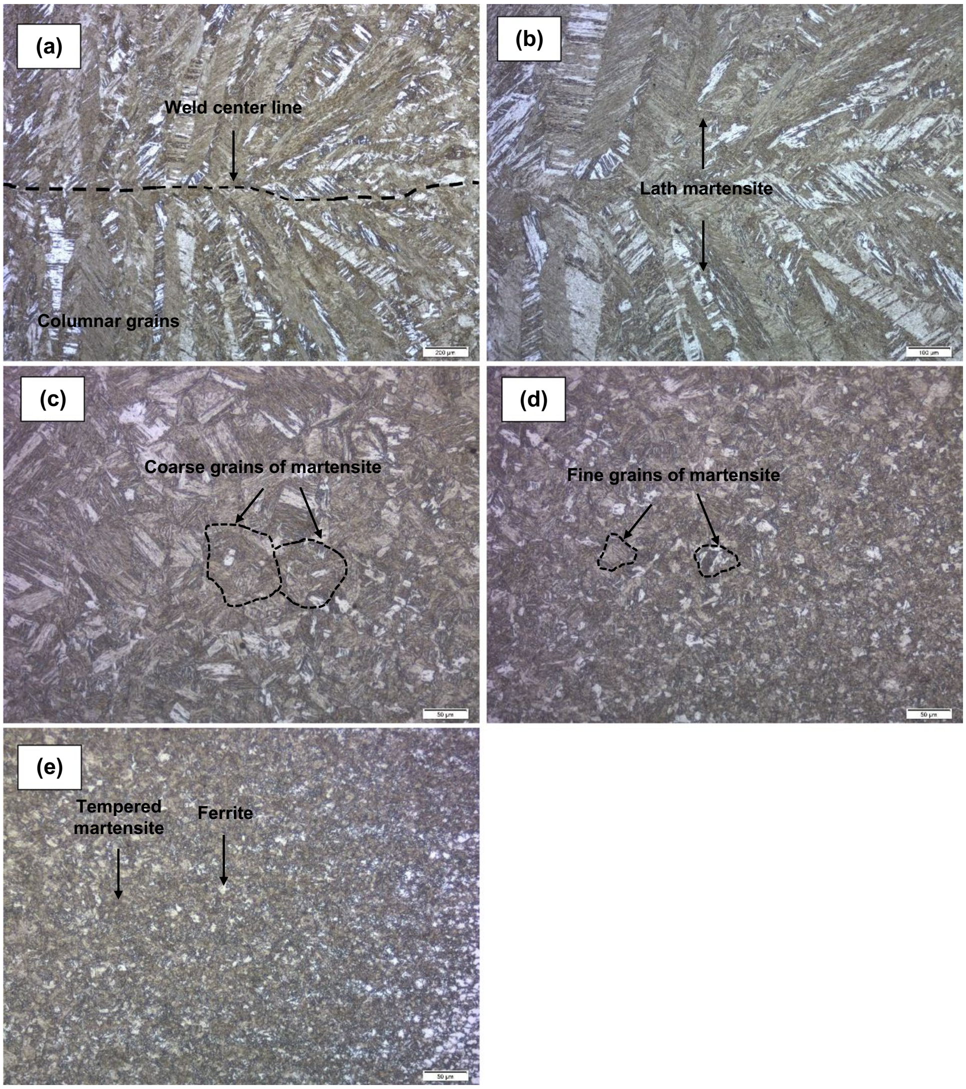

Fig. 4 The microstructure of different regions of single-pulse weld joint

to intensified heating of the nugget during the secondary pulse current.

3.2 Microhardness characteristics

Figure 6 shows the hardness profile of weld joints made via single pulse and double pulse RSW methods. In general, hardness decreased in the order of BM < FZ < HAZ in both types of welds. However, the hardness of HAZ decreased in order SCHAZ < CGHAZ < FGHAZ. The average hardness of BM is ~ 205 HV, SPW-FZ is ~ 410 HV, SPW-CGHAZ is ~ 424 HV, SPW-FGHAZ is ~ 440 HV, and SPW-SCHAZ is ~ 202 HV. Similarly, the average hardness of DPW-FZ is ~ 342 HV, DPW-CGHAZ is ~ 335 HV, DPW-FGHAZ is ~ 350 HV and DPW-SCHAZ is ~ 161 HV. Generally, resistance spot weldment generates a heterogeneous microstructure in line with the thermal weld cycle. It is well known that the microstructure has a significant effect on the hardness of the resistance spot weld joint of steel. Therefore, hardness variation across the weld joint is explained based on microstructure development. The higher hardness of the SPW-FZ (twice compared to BM) is attributed to the high hardenability of the base metal and the high cooling rate of the RSW process, which promoted martensitic transformation. SPW-CGHAZ and SPW-FGHAZ show higher hardness compared to SPW-FZ which is caused by the smaller grains of martensite containing fine laths. With a further increase in distance from the fusion line, the hardness decreased. The sudden drop of hardness in SPW-SCHAZ is caused by the tempering of the martensite present base metal. The hardness reduced by ~ 16.5% in DPW-FZ, ~ 20.9% in DPW-CGHAZ, 20.4% in DPW-FGHAZ, and ~ 20.2% in DPW-SCHAZ compared to corresponding weld zones of SPW joint. The significant reduction in hardness of the DPW joint caused by secondary heating resulting in the tempering of the martensite structure.

Fig. 5 Optical micrographs showing the microstructure of different regions of single pulse weld joint **a** FZ at low magnification, **b** FZ at high magnification, **c** CGHAZ, **d** FGHAZ, and **e** SCHAZ

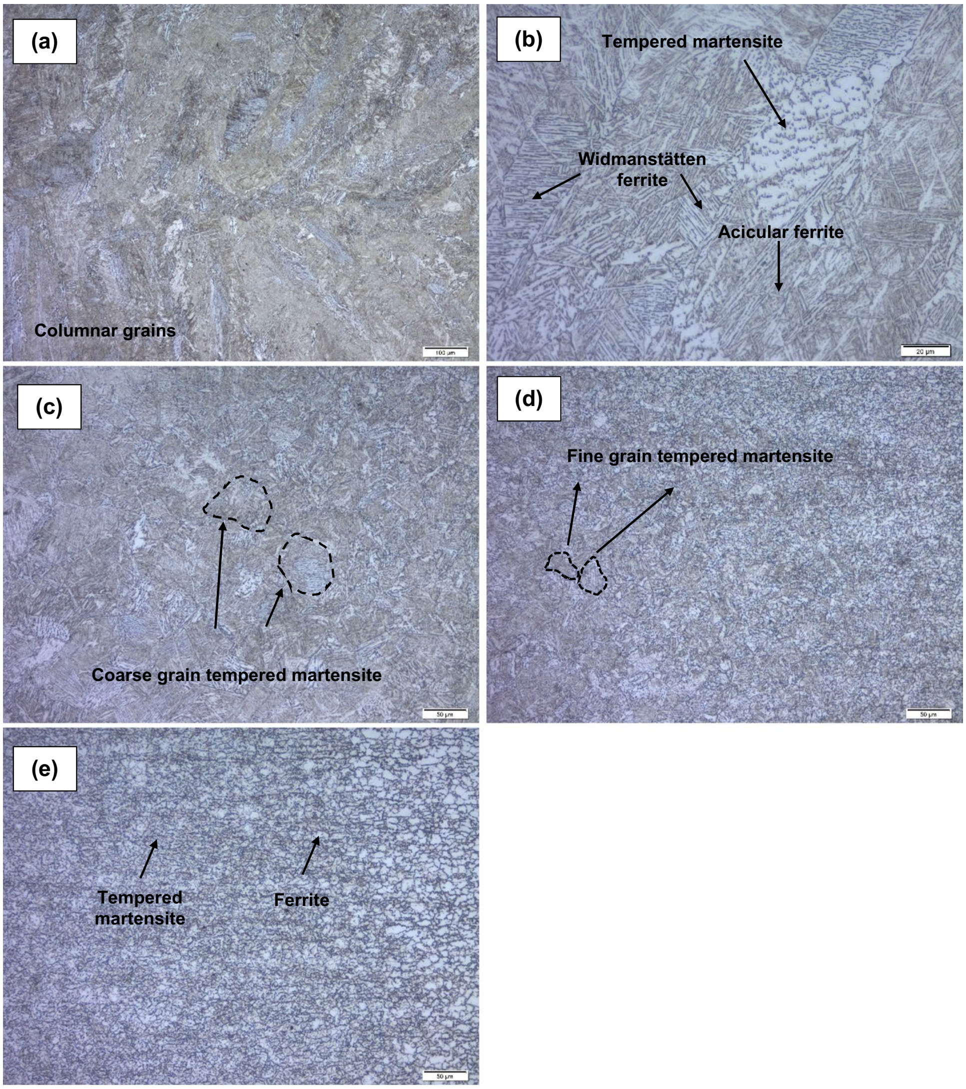

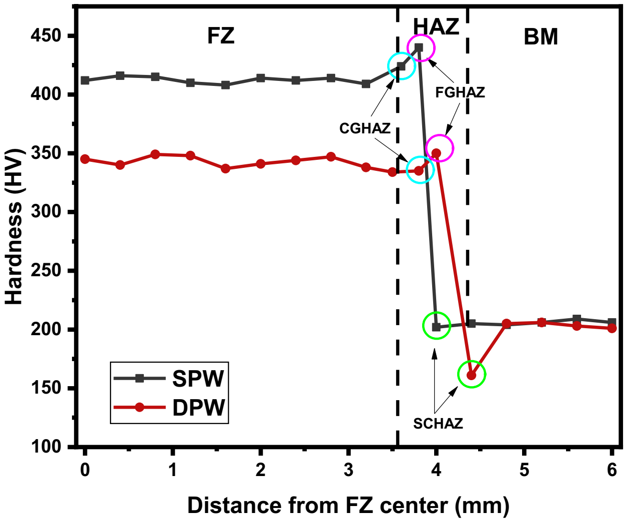

Fig. 6 Microhardness profile of single pulse welded and double pulse welded joints

3.3 Pre-tensile shear test performance

Figure 7 shows the quasi-static tensile shear load–displacement curves and the average peak load and failure energy value of single-pulse and double-pulse welded specimens. The double-pulse welded specimens produced a 15.6% higher peak load averaging 26.35 kN than the single-pulse welded specimens that averaged 22.8 kN. Similarly, double-pulse welded specimens produced 83.1% higher failure energy averaging 97.3 J than single-pulse welded specimens averaging 53.14 J. The cross-sections and fracture surface characteristics of the failed specimens are shown in Fig. 8. Single-pulse welded specimens failed via interfacial failure (IF) mode. In this failure mode, the crack propagated through the nugget centreline (refer to Fig. 8a), thus separating the joint into two pieces. Double pulse welded specimens failed via pullout failure (PF) mode. In this failure mode, nugget plugged from one sheet and remained intact with

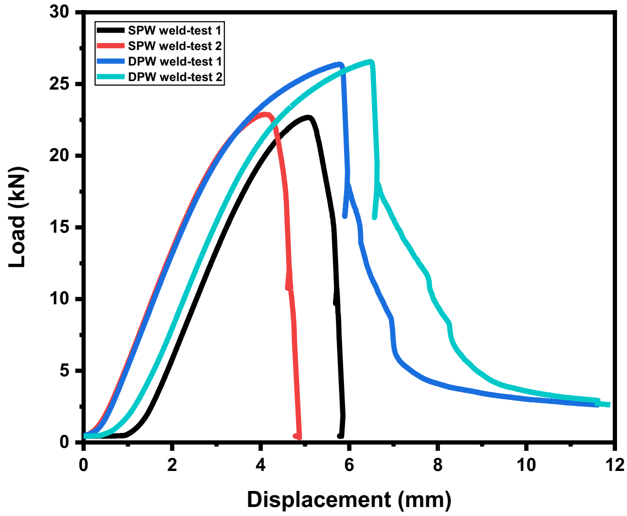

Fig. 7 Load–displacement curves and the average peak load of SPW and DPW welds

the second sheet (refer to Fig. 8b). The fracture surface of the single pulse welded joint exhibits micropores and torn bands (refer to Fig. 8c, e) which are characteristics of a typical cleavage fracture. During tensile shear loading, the crack initiated from the notch (which acts as pre-crack and stress concentration point) and propagated rapidly through the nugget center. The load suddenly drops to zero level with little plastic deformation (as indicated by load–displacement curves). The fracture surface of the double pulse welded joint exhibits dimples (refer to Fig. 8d., f) which are characteristics of a ductile fracture. During tensile shear loading, the crack is initiated from the BM/HAZ interface and then propagates around the nugget circumference, as shown in Fig. 8b, d. Although the global loading condition was tensile shear at the sheet/sheet plane, the tensile stresses developed at the nugget circumference. Therefore, failure occurred through rotation and preferential necking in the nugget circumference. The peak point in the load–displacement curves indicates the necking point. This necking in one of the sheets became more severe than in the other and hence resulted in

Fig. 8 Metallographic cross-section of the welds broken after quasi-static tensile shear test **a** SPW joint and **b** DPW joint. Fracture surface morphology **c**, **d** SPW joint and **d**, **e** DPW joint

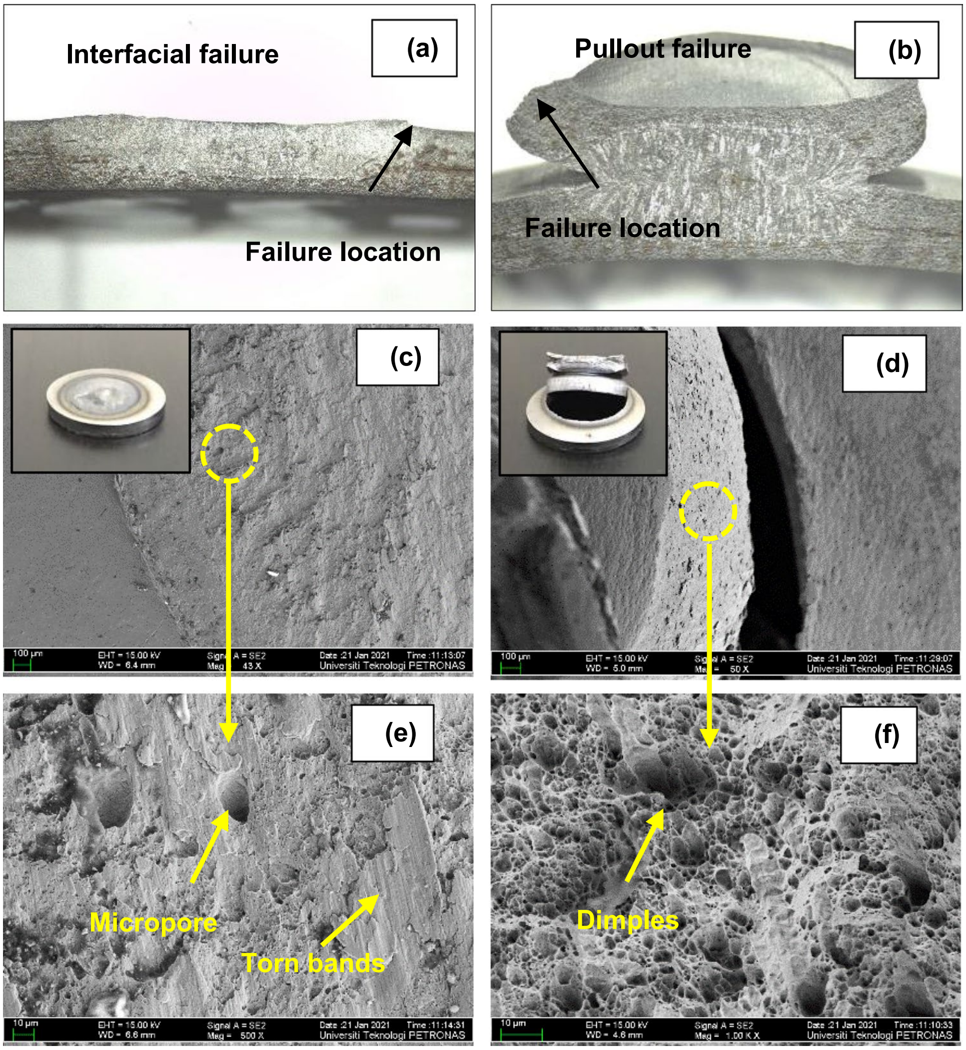

the withdrawal of nugget from one sheet. The load–displacement curve of the double-pulse welded joint has a long tail which corresponds to the post-necking due to the continued deformation. It is well known that during tensile shear loading necking tends to occur in the lowest hardness zone of automotive steel resistance spot weld [29]. As mentioned earlier, the lowest hardness occurred in the SCHAZ of the DPW welded joint. The severe martensite tempering in the SCHAZ after secondary heating caused softening which in turn reduced the strength of the HAZ, improved the onset of plastic deformation and hence encouraged the PF mode.

3.4 Fatigue performance

Figure 9 shows the maximum fatigue load vs. the number of cycles to the failure curve of SPW and DPW specimens. As can be seen, the overall trend of both types of welds is similar, with the number of cycles to failure (N_f) increased as the applied load decreased. However, DPW specimens withstand 10.8%, 22.7%, 1.8%, 158.7%, and 20.2% higher number of cycles than SPW specimens at an applied load of 2.3, 2.76, 3.45, 4.6, and 8.1 kN, respectively. The higher fatigue strength of DPW specimens can be attributed to two factors, i.e., the first being the large nugget size and the second being the higher toughness of the nugget. As the nugget size increased, the effective bonding area increased, which restricted the angular opening of the notches (present at the edges of the nugget) during cyclic loading, which in turn caused the lowering of stress concentration at the notch tip resulting in enhanced fatigue life [30]. In addition, the presence of acicular ferrite, Widmanstätten ferrite, and tempered martensite in the nugget microstructure improved the weld joint toughness resulting in enhanced resistance to crack propagation.

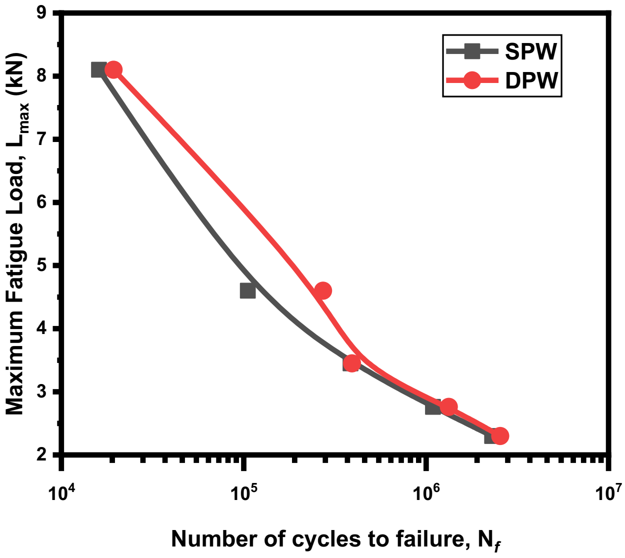

Fig. 9 Maximum fatigue load versus number cycles to failure curve

3.4.1 Fatigue failure mechanism

Figure 10 shows the photographs of fatigue failure of spot-welded specimens. As can be seen, the specimens failed via three types of mode indicated as Type-1, Type-2, and Type-3. Figure 11 shows the schematic illustration of crack initiation and propagation in three types of failure modes. In three types of failure modes, the crack is initiated from the notch tip. This is due to the fact that the notch tip experienced maximum stress during fatigue loading. After initiation, the crack path changed depending upon the local mechanical response of FZ and HAZ to the applied load. A detailed discussion of the fatigue failure mechanism is given as follows:

Type-1 failure mode Figure 12a shows the overview of the weld failed via Type-1 failure mode. This type of failure occurred only in SPW welded specimen at an applied load of 8.1 kN. As can be seen that the weld separated off into two pieces. The fracture surface shows two distinct regions (i) a flat region exhibiting torn bands at the outer periphery of the nugget (refer to Fig. 12b) and (ii) a rough region exhibiting microvoids coalescence at the center of nugget (refer to Fig. 12c). During cyclic loading, the weld nugget experienced shear stress in the longitudinal direction. The crack initiated on the interface between upper and lower sheets, i.e., at the notch tip. The arising bending moment results in kinking, and the crack propagated rapidly through the HAZ to the nugget. The relatively small nugget, the high microhardness due to the presence of brittle martensitic structure, and the formation of micropores in FZ of SPW weld nugget could not provide enough resistance to crack propagation. The synergistic effect of these factors promoted interfacial failure within nugget.

Type-2 failure mode This type of failure occurred in SPW welded specimens at an applied load of 2.3, 2.76, 3.45, and 4.6 and in DPW welded specimens at an applied load of 4.6 and 8.1 kN. Figures 13a and 14a show the overview of the SPW and DPW weld joints failed via Type 2 failure mode, respectively. As can be seen, weld joints exhibit partial plug-type failure in which some part of the nugget is pulled out from the sheet. During cyclic loading, the crack initiated from the root of the notch and then grew a short distance along the nugget perimeter, i.e., through HAZ to FZ. The crack then propagated in the transverse direction along the base metal sheet width on reaching the surface. The fracture surface exhibits two distinct regions (i) the middle area of the nugget showing striations (refer to Figs. 13b, c and 14b, c) and (ii) the bottom area with a flat surface (refer to

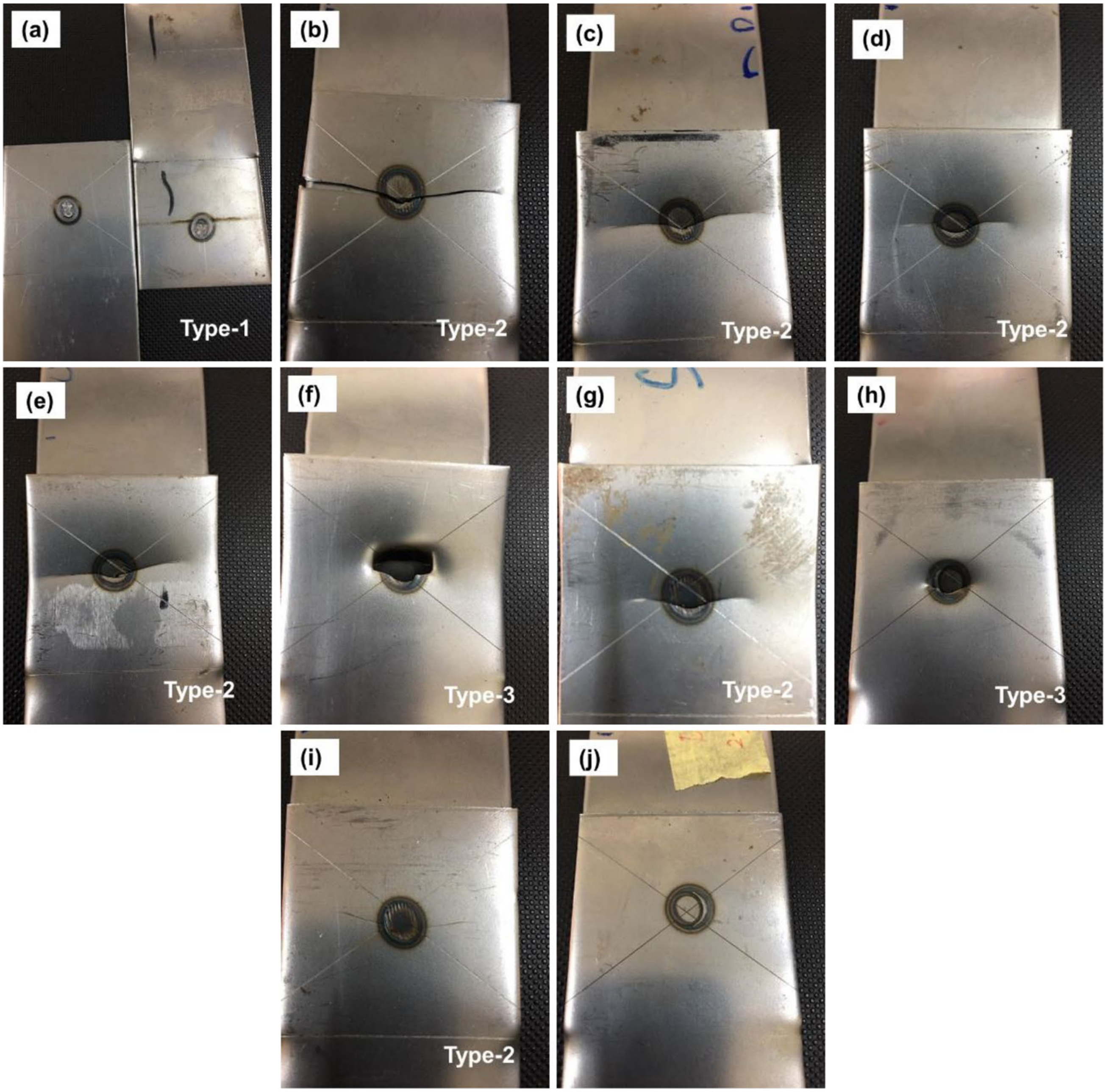

Fig. 10 Photographs of welds after fatigue testing (**a**, **c**, **e**, **g**, **i**) single pulse welded specimens failed under applied loads of 8.1, 4.6, 3.45,2.76, 2.3 kN, respectively, and (**b**, **d**, **f**, **h**) double pulse welded specimens failed under applied loads of 8.1, 4.6, 3.45,2.76, respectively. Note: double pulse welded specimen under applied load of 2.3 kN shows crack free surface

Figs. 13d and 14d). It is noteworthy that this type of failure occurred in SPW welded joint at relatively lower fatigue loads compared to DPW welded joint. This can be associated to the larger nugget size of DPW weld and higher fracture toughness, thus providing resistance to crack propagation even at high loads.

Type-3 failure mode This type of failure occurred only in DPW welded specimens subjected to an applied load of 2.76 and 3.45 kN. Figure 15a shows the overview of the failed broken weld. As can be seen, the broken welded joint exhibits a full plug failure. Again, this can be attributed to the higher fracture toughness of the DPW weld nugget which arrested crack propagation through the fusion zone. During cyclic loading, two cracks initiated directly from the notch on either side of the nugget and then proceeded through HAZ to the edge of the fusion zone. The fracture surface shows three distinct regions. In region-1, the striations

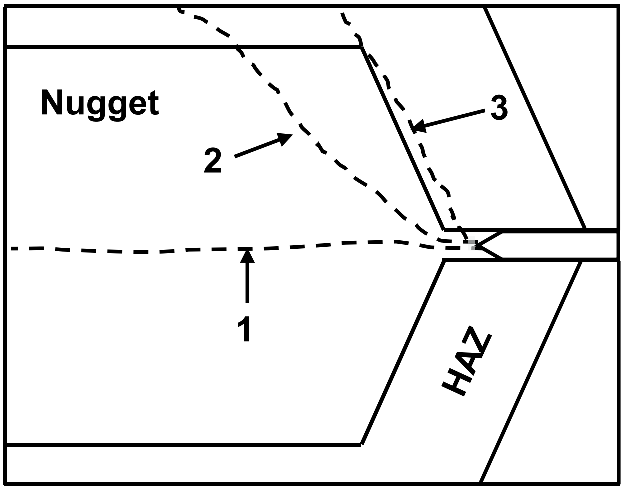

Fig. 11 Schematic illustration of fatigue crack propagation in Type-1, Type-2, and Type-3 failure

grew parallel to the applied load direction around the nugget circumference, while the striations grew perpendicular to the applied load direction in region-2 (refer to Fig. 15b). In region-3, the striations grew about 45° to the applied load direction (refer to Fig. 15c, d). Specimens that failed via Type-2 failure mode showed high fatigue strength. The plug failure is attributed to the higher toughness of the nugget. Ordoñez et al. [31] and Hilditch et al. [32] also showed that tempered martensite microstructure of the weld nugget improved the fracture toughness, thus reducing the fatigue damage and promoting plug type of failure in resistance spot weld of high-strength steels.

3.5 EBSD analysis

The EBSD images, inverse pole figures, and pole figures relating to the fusion zone of SPW and DPW welds are shown in Figs. 16 and 17, respectively. As can be seen, the DPW-FZ consists of small grains than SPW-FZ. Additionally, DPW-FZ grains show a random texture than those for SPW-FZ. As mentioned earlier, the SPW-FZ consists of large directionally solidified columnar grains resulting from the rapid cooling of molten metal during conventional RSW. In double pulse RSW, the post-weld heating cycle affected the microstructure of FZ, resulting in a refined grain structure. Primary columnar grains of FZ originated from the first heating cycle of the welding process were softened during the secondary heating cycle and were deformed due to force applied by electrodes.

In addition, SPW-FZ exhibits a strong texture with a maximum intensity of 6.482 toward {001}//TD, {111}//TD, and {110}//RD. The strong texture of SPW-FZ can be attributed to the directional solidification of columnar grains. The columnar grains grow preferentially in the direction of heat flow and are normal to the solid–liquid interface. On the other hand, DPW-FZ exhibits a relatively random texture with a maximum intensity of 4.512 corresponding to {111}//RD. The random texture of DPW-FZ can be attributed to post-weld heating resulting in recrystallization of grains.

3.5.1 Grain boundaries misorientation analysis

Figure 18 shows the misorientation angle distribution of the SPW-FZ and DPW-FZ grain boundaries. As can be seen, both welds show a high fraction of LAGBs ($\theta < 15°$) with strong distribution from 2.6 to 10° and a low fraction of HAGBs ($\theta > 15°$) with the strong distribution between 47.4 and 60.2° [33, 34]. It can be observed the fraction of LAGBs of DPW-FZ is ~ 24.5% lower than SPW-FZ. The high fraction of LAGBs in SPW-FZ can be associated to the high fraction of lath boundaries ($\theta = 2–5°$) produced within fully lath martensitic structure. The low fraction of LAGBs in DPW-FZ can be attributed to the partial recovery of laths. In double pulse RSW, during secondary heating (when temperatures reach ~ 650 °C), the lath boundary area drops significantly (as a result of the elimination of LAGBs) [35]. In addition, the deformation induced within softened grains

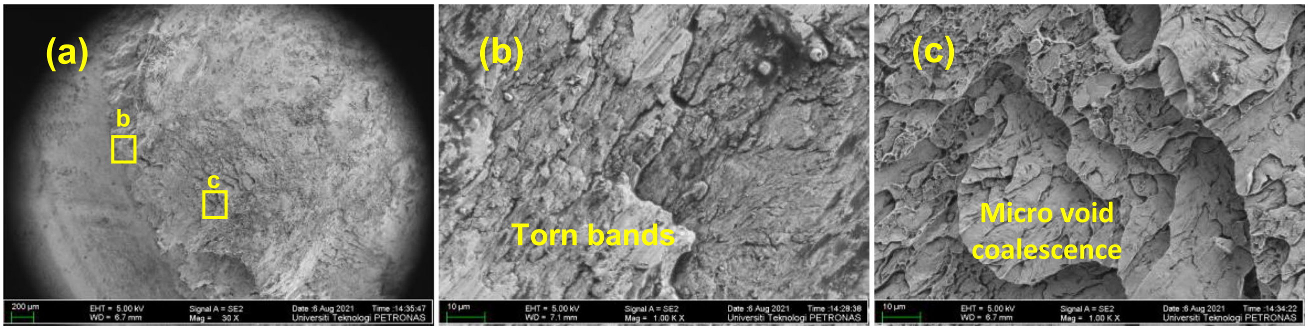

Fig. 12 Fracture surface morphology of the weld failed via Type-1 mode **a** overall view, **b** at outer ring of nugget, and **c** at the centre of nugget

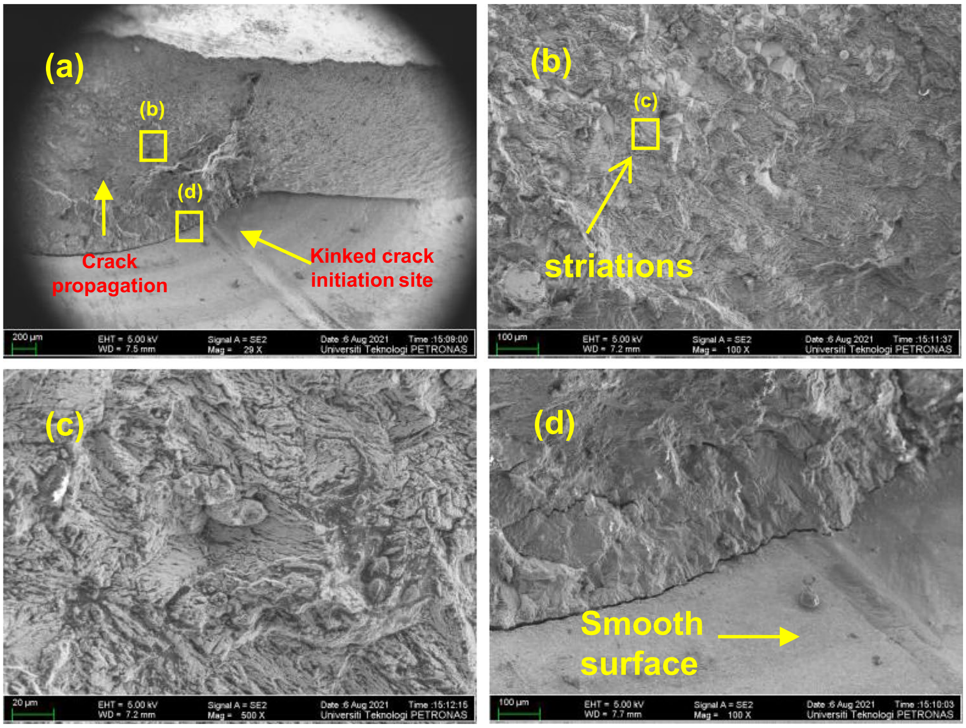

Fig. 13 Fracture morphology of the single pulse weld failed via Type-2 mode **a** overall view, **b** at the middle of nugget, **c** higher magnification image at the middle of nugget, and **d** at bottom of nugget

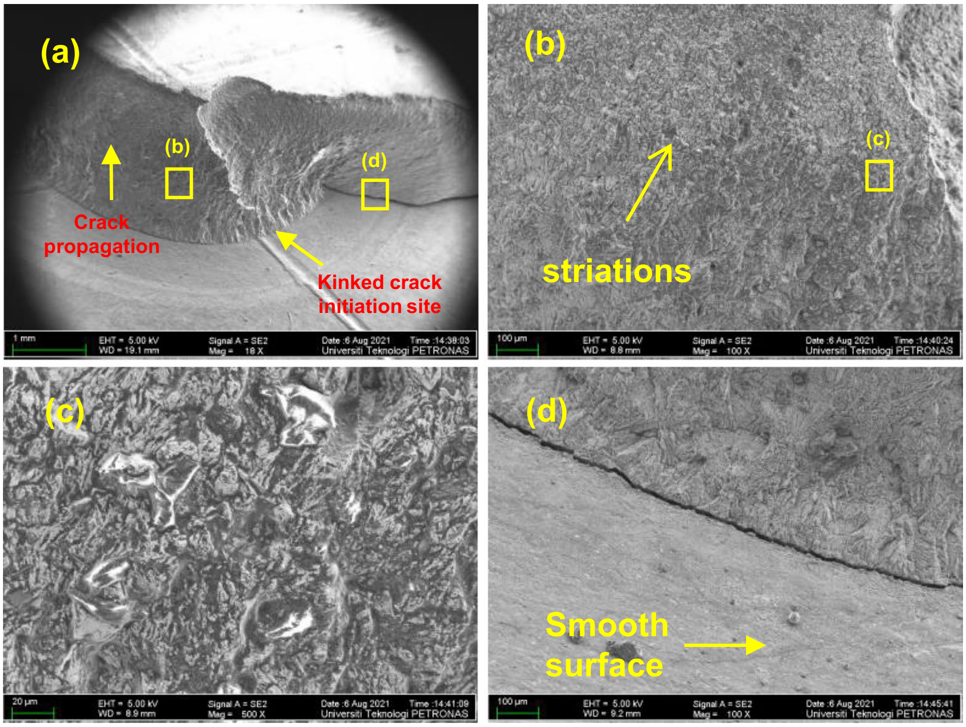

Fig. 14 Fracture morphology of the double pulse weld failed via Type-2 mode **a** overall view, **b** at the middle of nugget, **c** higher magnification image at the middle of nugget, and **d** at bottom of nugget

by electrodes transformed some of LAGBs to HAGBs. Thus, the lower fraction of LAGBs and a higher fraction of HAGBs of DPW-FZ can be attributed to recovery and recrystallization of lath martensite during rapid post-weld heating in comparison to SPW-FZ.

3.5.2 Effect of texture on fatigue strength of the welds

During cyclic loading, the crack initiated from the notch and then propagated from HAZ through the FZ of SPW specimens. With large columnar grains of brittle

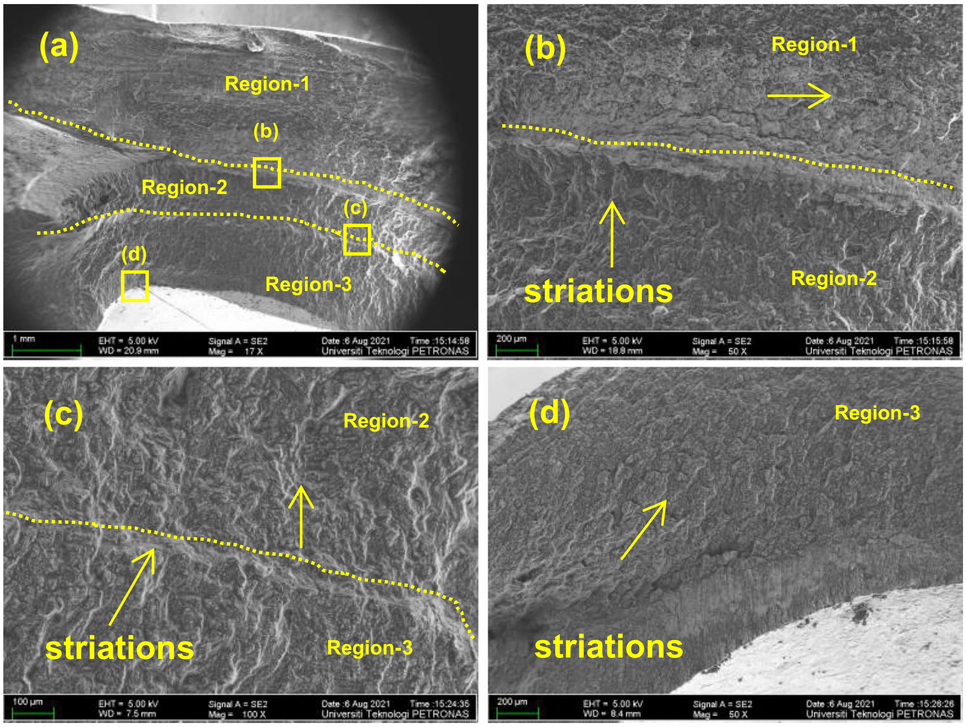

Fig. 15 Fracture morphology of the weld failed in Type-3 mode **a** overall view, **b** fracture surface at the middle of nugget, and **c**, **d** fracture surface at the bottom of the nugget

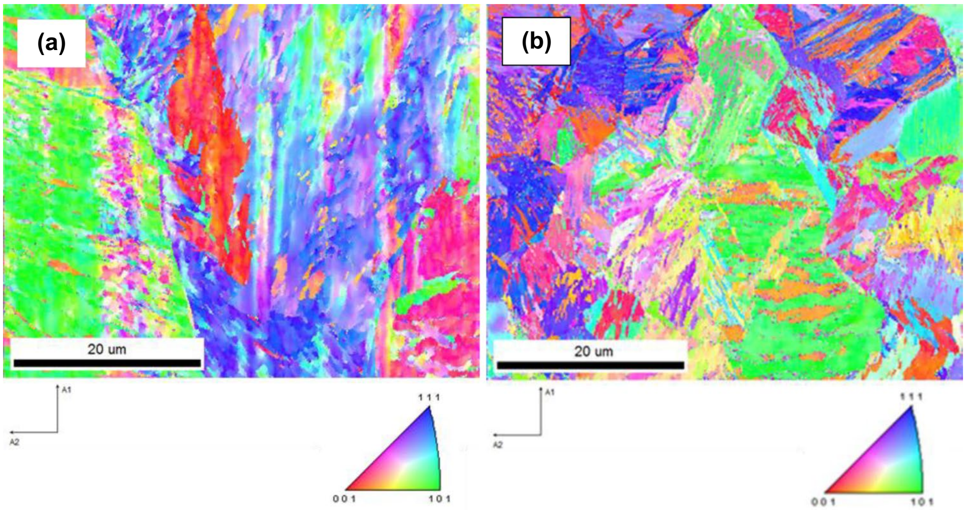

Fig. 16 EBSD image with inverse pole figure **a** SPW-FZ and **b** DPW-FZ

martensite containing a low fraction of HAGBs and with preferred orientation of grains, SPW-FZ exhibited low fracture toughness and provided a weak interface along the fusion line, making crack propagation easy, thus resulting in a low number of cycles in comparison to DPW specimens. In DPW specimens, the crack propagation was much arrested at the outer periphery of the nugget once it crossed over randomly orientated grains containing fraction HAGBs. During crack propagation, more energy was consumed, thus reducing the overall crack length and promoting plug-type failure.

3.6 Nanoindentation analysis

Automotive steel resistance spot welds usually constitute a complex microstructure gradient with various mechanical responses in a confined space. Microstructure gradient among the FZ, HAZ, and BM creates stress concentrations in the weld zone with the lowest strength or hardness. Therefore, understanding the mechanical behavior at a smaller scale is crucial in order to understand the bulk mechanical response and failure mechanism of welds. In this regard, the nanomechanical behavior of single-pulse

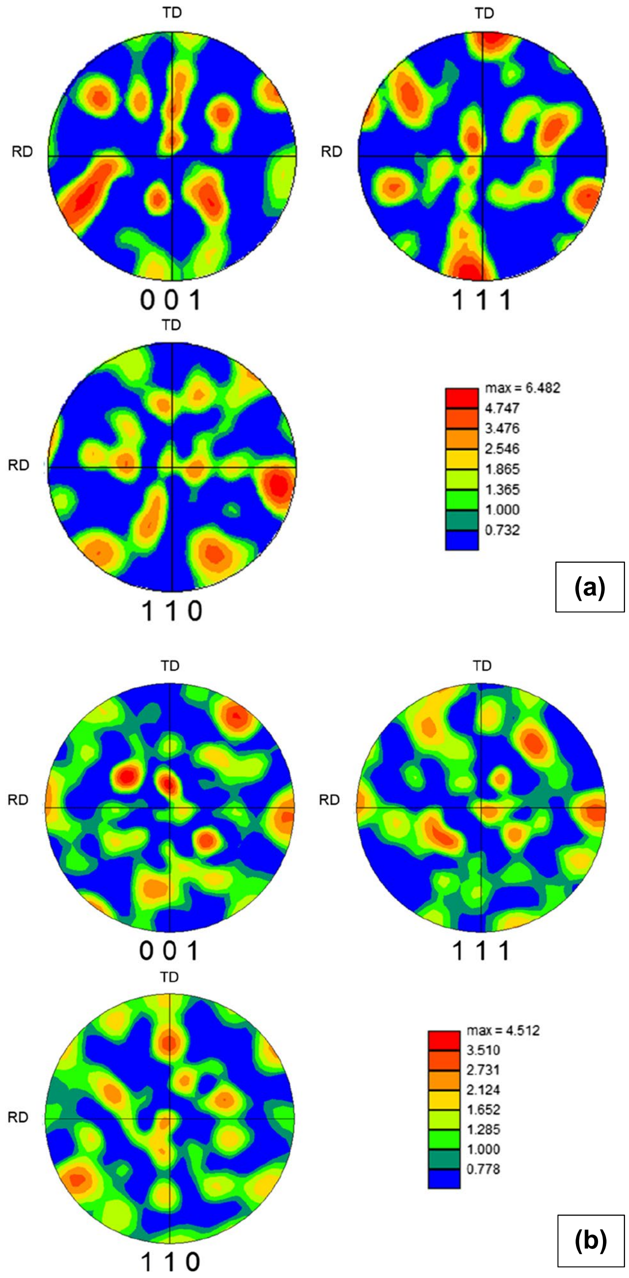

Fig. 17 Pole figures showing the grain orientation and texture intensity **a** SPW-FZ and **b** DPW-FZ

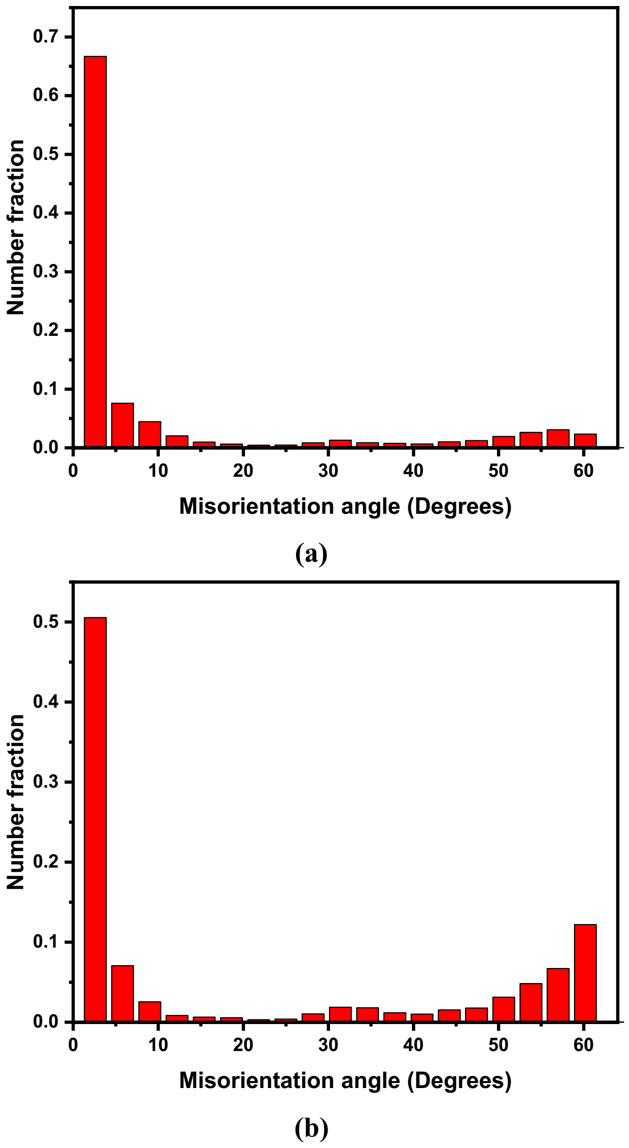

(a)

(b)

Fig. 18 Grain boundaries misorientation angle distribution **a** SPW-FZ and **b** DPW-FZ

and double-pulse welded joints was evaluated. The nanoindentation was performed in the fusion zone and failure location (FL, i.e., where failure originated during quasi-static tensile shear loading) to distinguish the change in mechanical response resulting from different metallurgical phases. It is noteworthy to mention here that SPW-FL corresponds to FGHAZ, while DPW-FL corresponds to SCHAZ. Figure 19 shows the SEM micrographs of the fusion zone and failure location of both types of weld. As can be observed, the microstructure of SPW-FZ and SPW-FL consists of martensitic structure, while DPW-FZ exhibits tempered martensite and DPW-FL exhibits ferrite and tempered martensite.

The nanoindentation load–displacement (*P*–*h*) curves are shown in Supplementary Fig. 1. According to *P*–*h* curves, SPW-FZ exhibits lower displacement than SPW-FL, implying that martensite formed in columnar grains is easier to penetrate than martensite formed in equiaxed grains. This can be attributed to fine laths of martensite of failure location, i.e., FGHAZ, resulting in higher hardness. On the other hand, DPW-FZ shows lower displacement than DPW-FL. DPW-FL microstructure consisted of softer phases, i.e., ferrite and tempered martensite, compared to the microstructure of DPW-FZ consisted of fully tempered martensite resulting in lower deformation. Figure 20 shows

Fig. 19 SEM micrographs showing the microstructure of fusion zone and failure location **a** SPW-FZ (M), **b** SPW-FL, **c** DPW-FZ, and **d** DPW-FL

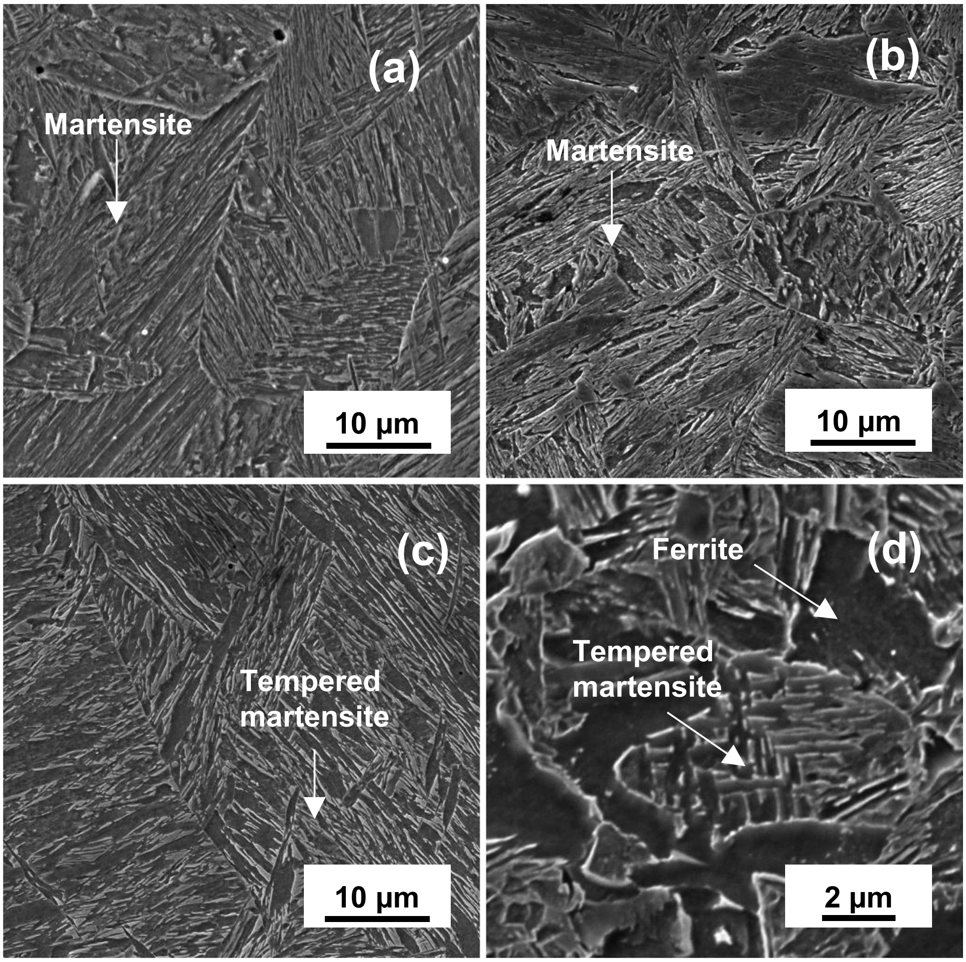

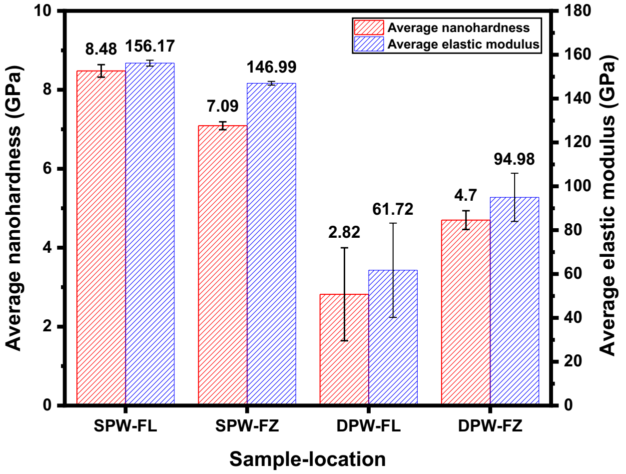

Fig. 20 Average nanohardness and elastic modulus of failure location and fusion zone of single pulse and double pulse weld joints

the calculated average nanohardness and elastic modulus of the welds. The average nanohardness and elastic modulus of DPW-FL are 66.7% lower than SPW-FL, respectively, while the average nanohardness and elastic modulus of DPW-FZ are 33.7% lower than SPW-FZ. The reduction of nanohardness and elastic modulus is attributed to the tempering of martensitic structure in the corresponding weld zone of the double-pulse weld joint. Therefore, the mechanical performance of the double-pulse weld joint can also be attributed to softening caused by tempered martensite formed in the fusion zone and failure location, which improved the weld toughness.

4 Conclusion

Based on the analysis of results, the following conclusions are drawn:

1. The nugget diameter of weld joint increased by 13.8% made via the DPW method compare to SPW weld joint. The microstructure of SPW-FZ consisted of large columnar grains of brittle martensite phase and showed preferred orientation. On the other hand, the microstructure of DPW-FZ consisted of columnar grains of tem-

pered martensite along with a small amount of acicular ferrite and Widmanstätten ferrite and showed random orientation.

2. Under quasi-static tensile shear loading, specimens via double pulse RSW method showed 15.6% and 83.1% average higher peak load and failure energy compare to specimens made via single pulse RSW method.
3. Under fatigue loading, specimens made via the double pulse RSW method withstand 10.8%, 22.7%, 1.8%, 158.7%, and 20.2% higher number of cycles than specimens made via single pulse RSW method at an applied load of 2.3, 2.76, 3.45, 4.6, and 8.1 kN, respectively.
4. Weld joint made via the double pulse RSW method showed 33.7% and 66.7% lower average nanohardness and elastic modulus of fusion zone and failure location, respectively than SPW weld joint.
5. The improvement in the mechanical performance of the double pulse weld is attributed to multi factors, i.e., (i) enlarged nugget size resulting in a larger bonding area between the sheets, (ii) formation of randomly orientated grains with a high fraction of HAGBs of FZ resulting in improved nugget resistance to crack propagation, and (iii) improved weld toughness due to tempering of martensite in the fusion zone and failure location.

Supplementary information The online version contains supplementary material available at https://doi.org/10.1007/s00170-022-10704-3.

Acknowledgements The authors would like to acknowledge the Bloxwich Sdn Bhd Malaysia for providing a resistance spot welding facility. The authors would also like to acknowledge High-Tech Instrument Sdn Bhd Malaysia for providing a Backscattered Electron Diffraction facility and MIMOS Sdn Bhd Malaysia for providing a nanoindentation facility. The authors are also thankful to Mr. Nasrizal for his assistance in conducting fatigue tests at UNiKL Malaysia.

Funding This work was supported by the University Teknologi PETRONAS (UTP) Malaysia grant [015LCO-129]. Mokhtar Awang received the grant from UTP.

Data availability The data that support the findings of this study are available from the corresponding author upon reasonable request.

Code availability Not applicable.

Declarations

Ethics approval The work contains no libelous or unlawful statements, does not infringe on the rights of others or contains material or instructions that might cause harm or injury.

Consent to participate The authors declared their approval to participate in the submitted manuscript.

Consent for publication All authors have given their permission for publishing this work.

Competing interests The authors declare no competing interests.

References

1. Lesch C, Kwiaton N, Klose FB (2017) Advanced high strength steels (AHSS) for automotive applications – tailored properties by smart microstructural adjustments steel. Res Int 88:1700210
2. Fonstein N (2017) Dual-phase steels. In: Rana R, Singh SB (eds) Automotive steels. Woodhead Publishing, pp 169–216
3. Lai Q et al (2016) Influence of martensite volume fraction and hardness on the plastic behavior of dual-phase steels: experiments and micromechanical modeling. Int J Plast 80:187–203
4. Demeri MY (2013) Dual Phase Steels In: MY Demeri (ed) Advanced high-strength steels: science, technology, and applications, United States: ASM International, pp 95–105
5. Soomro IA, Pedapati SR, Awang M (2021) A review of advances in resistance spot welding of automotive sheet steels: emerging methods to improve joint mechanical performance. Int J Adv Manuf Technol. https://doi.org/10.1007/s00170-021-08002-5
6. Vignesh K, Perumal AE, Velmurugan P (2017) Optimization of resistance spot welding process parameters and microstructural examination for dissimilar welding of AISI 316L austenitic stainless steel and 2205 duplex stainless steel. Int J Adv Manuf Technol. https://doi.org/10.1007/s00170-017-0089-4
7. Goodarzi M, Marashi SPH, Pouranvari M (2009) Dependence of overload performance on weld attributes for resistance spot welded galvanized low carbon steel. J Mater Process Technol 209:4379–4384
8. Ertas AH, Vardar O, Sonmez FO, Solim Z (2008) Measurement and assessment of fatigue life of spot-weld joints. J Eng Mater Technol 131:011011
9. Kang KW (2014) Vibration fatigue analysis of spot welded component considering change of stiffness due to fatigue damage. J Korea Converg Soc 5:1–8
10. Miller KW, Chao YJ, Martinez A, Zhu X, Liu S, Wang PC (2003) Quasi-static and impact strength of fatigue damaged spot welds. SAE Int. https://doi.org/10.4271/2003-01-0610
11. Kim DH, Kim HK (2009) Fatigue strength evaluation of cross-tension spot weld joints of cold rolled mild steel sheet. Mater Des. https://doi.org/10.1016/j.matdes.2009.01.002
12. Pouranvari M (2012) Susceptibility to interfacial failure mode in similar and dissimilar resistance spot welds of DP600 dual phase steel and low carbon steel during cross-tension and tensile-shear loading conditions. Mater Sci Eng A. https://doi.org/10.1016/j.msea.2012.03.040
13. Sawanishi C et al (2013) Mechanical properties and microstructures of resistance spot welded DP980 steel joints using pulsed current pattern. Sci Technol Weld Join 19:52–59. https://doi.org/10.1179/1362171813y.0000000165
14. Chabok A, van der Aa E, De Hosson JTM, Pei YT (2017) Mechanical behavior and failure mechanism of resistance spot welded DP1000 dual phase steel. Mater & Des 124:171–182. https://doi.org/10.1016/j.matdes.2017.03.070
15. Eftekharimilani P, van der Aa EM, Hermans MJM, Richardson IM (2017) Microstructural characterisation of double pulse resistance spot welded advanced high strength steel. Sci Technol Weld Join. https://doi.org/10.1080/13621718.2016.1274848
16. Sajjadi-Nikoo S, Pouranvari M, Abedi A, Ghaderi AA (2017) In situ postweld heat treatment of transformation induced plasticity steel resistance spot welds. Sci Technol Weld Join. https://doi.org/10.1080/13621718.2017.1323174
17. Soomro IA, Pedapati SR (2019) Application of in situ post weld heat treatment using double pulse technology and its effect on microstructure and mechanical performance of resistance spot welded HSLA350 steel. Int J Adv Manuf Technol. https://doi.org/10.1007/s00170-019-04569-2

18. Aghajani H, Pouranvari M (2019) Influence of in situ thermal processing strategies on the weldability of martensitic stainless steel resistance spot welds: effect of second pulse current on the weld microstructure and mechanical properties. Metall Mater Trans A. https://doi.org/10.1007/s11661-019-05443-2
19. Pouranvari M, Aghajani H, Ghasemi A (2020) Enhanced mechanical properties of martensitic stainless steels resistance spot welds enabled by in situ rapid tempering. Sci Technol Weld Join. https://doi.org/10.1080/13621718.2019.1641962
20. Liu XD, Xu YB, Misra RDK, Peng F, Wang Y, Du YB (2019) Mechanical properties in double pulse resistance spot welding of Q&P 980 steel. J Mater Process Technol. https://doi.org/10.1016/j.jmatprotec.2018.08.018
21. Oliver WC, Pharr GM (1992) An improved technique for determining hardness and elastic modulus using load and displacement sensing indentation experiments. J Mater Res. https://doi.org/10.1557/JMR.1992.1564
22. Soomro IA, Pedapati SR, Awang M (2021) Optimization of postweld tempering pulse parameters for maximum load bearing and failure energy absorption in dual phase (DP590) steel resistance spot welds. Mater Sci Eng: A 803:140713. https://doi.org/10.1016/j.msea.2020.140713
23. Pouranvari M, Marashi SPH (2013) Key factors influencing mechanical performance of dual phase steel resistance spot welds. Sci Technol Weld Join. https://doi.org/10.1179/136217109x12590746472535
24. Pouranvari M (2011) Effect of resistance spot welding parameters on the HAZ softening of DP980 ferrite-martensite dual phase steel welds. World Appl Sci J 15:1454–1458
25. Dong WC, Wen MY, Pang HY, Lu SP (2020) Effect of post-weld tempering on the microstructure and mechanical properties in the simulated HAZs of a high-strength-high-toughness combination marine engineering steel. Acta Metall Sin. https://doi.org/10.1007/s40195-019-00954-8
26. Zhong N, Liao X, Wang M, Wu Y, Rong Y (2011) Improvement of microstructures and mechanical properties of resistance spot welded DP600 steel by double pulse technology. Mater Trans. https://doi.org/10.2320/matertrans.M2011135
27. Liao X, Wang X, Guo Z, Wang M, Wu Y, Rong Y (2010) Microstructures in a resistance spot welded high strength dual phase steel. Mater Charact. https://doi.org/10.1016/j.matchar.2009.12.018
28. Meshkov YY, Pereloma EV (2012) The effect of heating rate on reverse transformations in steels and Fe-Ni-based alloys. In: Pereloma E, Edmonds DV (eds) Phase Transformations in Steels. Woodhead Publishing, pp 581–618
29. Pouranvari M, Ranjbarnoodeh E (2013) Failure mode of HSLA/DQSK dissimilar steel resistance spot welds. Ironmak Steelmak. https://doi.org/10.1179/1743281212y.0000000044
30. Banerjee P, Sarkar R, Pal TK, Shome M (2016) Effect of nugget size and notch geometry on the high cycle fatigue performance of resistance spot welded DP590 steel sheets. J Mater Process Technol. https://doi.org/10.1016/j.jmatprotec.2016.07.023
31. Ordoñez JH, Ambriz RR, García C, Plascencia G, Jaramillo D (2019) Overloading effect on the fatigue strength in resistance spot welding joints of a DP980 steel. Int J Fatigue. https://doi.org/10.1016/j.ijfatigue.2018.12.026
32. Hilditch TB, Speer JG, Matlock DK (2007) Effect of susceptibility to interfacial fracture on fatigue properties of spot-welded high strength sheet steel. Mater Des. https://doi.org/10.1016/j.matdes.2006.10.019
33. Abbasi M, Bagheri B, Abdollahzadeh A, Moghaddam AS (2021) A different attempt to improve the formability of aluminum tailor welded blanks (TWB) produced by the FSW. Int J Mater Form 14:1189–1208. https://doi.org/10.1007/s12289-021-01632-w
34. Bagheri B, Abbasi M, Dadaei M (2020) Mechanical behavior and microstructure of AA6061-T6 joints made by friction stir vibration welding. J Materi Eng Perform 29:1165–1175. https://doi.org/10.1007/s11665-020-04639-7
35. Krauss G (2012) Tempering of martensite in carbon steels. In: Pereloma E, Edmonds DV (eds) Phase transformations in steels. Woodhead Publishing, pp 126–150